

Husimi-driven many-body systems realised with Bose-Einstein condensates

B.J. Mommers,^{1,2} A. Pritchard,^{1,2} T.A. Bell,^{1,2} R.N. Kohn, Jr.,³ S.E. Olson,⁴ M. Baker,^{5,2,1} and M.W.J. Bromley^{6,2}

¹*Centre for Engineered Quantum Systems, The University of Queensland, St Lucia, Australia*

²*School of Mathematics and Physics, The University of Queensland, St Lucia, Australia*

³*Space Dynamics Laboratory, Albuquerque, New Mexico 87106, USA*

⁴*Air Force Research Laboratory, Kirtland AFB, New Mexico 87117, USA*

⁵*Quantum Technologies, Cyber and Electronic Warfare Division, Defence Science and Technology Group, Brisbane, Australia*

⁶*School of Sciences, University of Southern Queensland, Toowoomba, Australia*

Quantum systems with exact analytic solutions are rare, with most systems of interest requiring perturbative or other approximate methods to produce theoretical models. Husimi’s 1953 solution to the Schrödinger equation for the linearly driven (see-saw) harmonic oscillator results in an exact solution for a wavepacket spatially translated but otherwise unperturbed by the driving force. In this work, we consider this Husimi driving scheme applied to a Bose-Einstein condensate (BEC), and further extend the theoretical solution to include interacting many-body systems in arbitrary states. We experimentally implement this solution in both optically- and magnetically-trapped BEC systems, subject to resonant or off-resonant driving by a linear magnetic potential. The observed trajectories of the centre-of-mass agree with theory, showing minimal excitation of the condensate. Based on these results, we propose Husimi driving as a platform for precision control of one-body, few-body, and many-body systems, and demonstrate its application to high-fidelity condensate transport at 72 times faster than adiabatic speeds. We demonstrate the platform’s utility in trap frequency measurement and introduce a Husimi driving-based scheme for atom interferometry.

I. INTRODUCTION

Few quantum systems are exactly solvable, especially many-body systems. In 1953 Husimi outlined the Gaussian-based solution to the one-dimensional Schrödinger equation for the forced quantum oscillator — a single particle in a harmonic potential subject to variations [1]. Two scenarios were considered by Husimi: changing the trapping potential strength and/or including a spatially linear driving potential of configurable strength. Solving the first scenario has attracted the most attention as it corresponds to a time-dependent trapping frequency variation [2–6], which finds application throughout quantum physics [7, 8]. The second scenario, through an additional driving force, is also known to admit solutions [7, 9–11]. In this work we consider the second scenario, with fixed harmonic trapping frequency, and a monochromatic “see-saw” modulation of the linear potential (see Fig. 1). From hereon we call this Husimi driving, which has centre-of-mass oscillations that are known to preserve initial states [1, 7, 12–15]. We extend this theoretically and realise experimentally using Bose-Einstein condensates to establish Husimi driving as a platform for precise control of quantum systems.

A key feature of the Husimi driving platform, as shown here, is enabling fast, excitation-free transport of BECs and other quantum systems. Such transport has been a long sought-after goal of quantum control [16] and has applications throughout quantum information, quantum simulation, and towards developing atomtronics-based applications [17]. Existing approaches to ultracold atom transport can be grouped into three main categories: (1) magnetic conveyor methods, where either magnetic coils are mechanically translated [18–20] or the electrical cur-

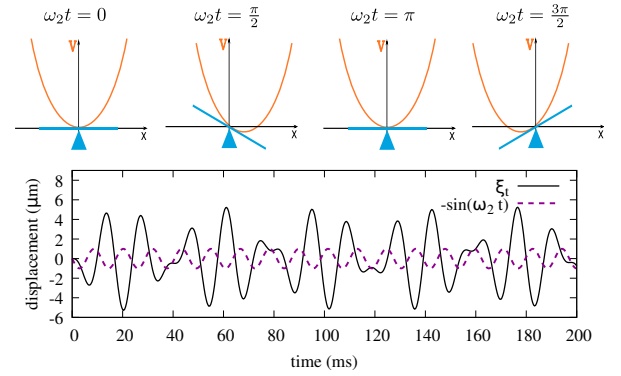


FIG. 1. (color online) Top: Schematic illustration of Husimi “see-saw” driving. The combination of a fixed harmonic trap with an oscillating linear potential, $V(x, t) = \frac{1}{2}\omega_1^2 x^2 - x \sin(\omega_2 t)$, can be visualised as a harmonic trap balancing on an oscillating see-saw (and not a side-to-side translation of the trap). Bottom: Analytic centre-of-mass displacement (black solid line) with the driving function $-\sin(\omega_2 t)$ (purple dashed line). A chosen frequency ratio $\omega_2/\omega_1 = \sqrt{2}$ results in aperiodic motion of the centre-of-mass [15]. Units were chosen for ease of comparison with experimental data. The corresponding field gradient from Eqn. 6 is $b_x = 0.85\text{G/cm}$.

rents between adjacent pairs of coils are sequenced [21–23]; (2) optical lattice methods [24]; or (3) translation of a rigid optical trap by various methods including optical tweezers [25–27], focus-tunable lenses [28], and translation of optics [29]. For fast transport tasks, spatial translation of rigid potentials has received the most attention, with the field of shortcuts to adiabaticity (STA) using invariant-based methods [30–34], reverse engineering [35], and control theory [36–40] to optimise rigid po-

tential trajectories for high transport speed and minimal excitation. BEC transport, however, has received comparatively little attention in terms of experimental fast transport implementations. Transport of a condensate via optical lattice methods [41, 42] and optical tweezers [27] have both been demonstrated – though unwanted excitations remained. Proposed STA methods promise improvements in BEC fast transport [32, 36, 40, 43], however, much of this theoretical work remains untested in BEC experiments, with some STA designs found to be unsuitable for experimental use [25].

We experimentally demonstrate Husimi driving with BECs using two harmonic trapping methods; an optical dipole and all-magnetic potential. Building on the basic demonstration of Husimi driving with BECs, we additionally propose and demonstrate a proof-of-concept method for using Husimi driving to achieve fast, excitation-free BEC transport – the first of multiple applications that can be derived from the Husimi driving platform. Our experimental demonstrations are theoretically underpinned by our generalisation of Husimi’s original single-particle solution to the many-body Schrödinger equation, in agreement with the Harmonic Potential theorem (HPT) [44]. The many-body solution shows that Husimi driving is equally effective for manipulating ultracold gases, BECs, and other many-body quantum systems. We show that Husimi’s original driving solution extends to interacting many-body systems in agreement with the HPT and can be further extended to include arbitrary states. For eigenstates, the centre-of-mass trajectory follows an analytic form, allowing for the validation of our experimental implementations.

The analytic centre-of-mass trajectory also provides an alternative, high-precision method for determining the trapping frequency of an experimental system. The current standard experimental method involves modulating the trap frequency to find a parametric resonance, which causes appreciable heating of the condensate [45]. We demonstrate Husimi trajectory fitting as a viable alternative to parametric heating methods, and discuss techniques to minimise the data required. Lastly, we consider the application of Husimi driving to interferometric schemes, both for future validation of the phase coherence of a condensate after transport, and for performing rotation measurements.

II. THEORY

Building on Husimi’s derivation [1], which used the 1-D Schrödinger equation, we instead adopt the 1-D Gross-Pitaevskii equation (GPE),

$$i\hbar \frac{\partial \psi}{\partial t} = \left(-\frac{\hbar^2}{2m} \frac{\partial^2}{\partial x^2} + V(x, t) + g|\psi|^2 \right) \psi, \quad (1)$$

which describes the evolution of the condensate order parameter $\psi(x, t)$. The contact interaction parameter g quantifies the s -wave atom-atom scattering strength [46].

The GPE is a nonlinear Schrödinger equation (NLSE) which describes low-temperature condensate dynamics.

We focus on solutions where the external potential consists of a static harmonic trap with a modulated linear component, $V(x, t) = \frac{1}{2}m\omega_1^2 x^2 - Axf(t)$, where A represents the modulation amplitude, $f(t)$ the modulation function, and m the atomic mass. This potential effectively spatially translates side-to-side and energetically decreases and increases, which is best seen re-written as

$$V(x, t) \equiv \frac{1}{2}m\omega_1^2 \left(x - \frac{Af(t)}{m\omega_1^2} \right)^2 - \frac{A^2 f^2(t)}{2m\omega_1^2}, \quad (2)$$

which shows that the Husimi see-saw potential is distinct from translating a rigid harmonic potential.

Following Husimi’s method, the order parameter $\psi(x, t)$ is analytically solved using $f(t) = \sin(\omega_2 t)$, Eqn. 1, Eqn. 2, and the transformation $x' = x - \xi(t)$ [47]. The transformed NLSE contains two additional terms. The first term vanishes provided $\xi(t)$ satisfies the classical forced oscillator equation of motion $m\ddot{\xi} + m\omega_1^2 \xi = Af(t)$, implying ξ can be physically interpreted as the time-dependent centre-of-mass coordinate $\langle x \rangle$. Introducing the global phase factor $Et = \int_0^t \frac{1}{2}m\dot{\xi}^2 - \frac{1}{2}m\omega_1^2 \xi^2 + A\xi f(t) dt$ then removes the second term. Given these constraints, the coordinate-transformed NLSE reduces to the NLSE solution for a static harmonic trap, akin to the original single-particle result, with the solution [47]

$$\psi(x, t) = \chi(x - \xi, t) \exp \left[i\dot{\xi}(x - \xi)/\hbar + iEt/\hbar \right]. \quad (3)$$

The initial state evolves as $\chi(x - \xi, t)$ according to its solution in a stationary oscillator potential [1].

The non-resonant $\omega_1 \neq \omega_2$ centre-of-mass oscillation is determined here using Husimi’s method via the classical oscillator solution, viz.

$$\xi(t) = \frac{A}{m(\omega_1^2 - \omega_2^2)} \left[\sin(\omega_2 t) - \frac{\omega_2}{\omega_1} \sin(\omega_1 t) \right]. \quad (4)$$

The solution for the resonant case $\omega = \omega_1 = \omega_2$ is

$$\xi(t) = \frac{A}{2m\omega^2} [\sin(\omega t) - \omega t \cos(\omega t)]. \quad (5)$$

These results also hold for the full 3-D NLSE as Husimi-driving will not excite additional modes beyond those already in the underlying NLSE dynamics $\chi(x - \xi, y, z, t)$ [47].

Furthermore, these results are readily generalised for the N -particle Hamiltonian [47]. Applying the same coordinate transformation produces a result consistent with the Harmonic Potential Theorem for many-body systems [44]. The solution for interacting gases in a harmonic potential with a uniform linear field can be separated into the relative motion of the centre-of-mass and the stationary many-body eigenstate – the main result of the HPT. Additionally, this is true for arbitrary states satisfying the many-body Schrödinger equation in the coordinate system co-moving with $\xi(t)$ – they continue to

evolve locally, independent of the Husimi driving [47]. We anticipate that the atomic cloud width should remain constant in all directions during Husimi experiments - an expectation our results validate. This decoupling of the centre-of-mass and collective excitations under Husimi driving enables precision control of quantum many-body systems including for transport protocols with zero net energy transfer between the driving field and the system.

III. EXPERIMENT I - OPTICAL DIPOLE TRAP

Our optical dipole BEC apparatus is described in Refs. [48, 49]. Condensates of ^{87}Rb were prepared in the $|F, m_F\rangle = |1, -1\rangle$ spin-state, in a 3-D optical trap formed using two orthogonal 1064 nm Gaussian beams. A horizontally propagating and elliptically focused sheet beam confines against gravity, with $1/e^2$ waists of 1.25 mm (in x) and $27\text{ }\mu\text{m}$ (in z), giving an estimated vertical trap frequency $\omega_z \approx 2\pi \cdot 140\text{ Hz}$. Cylindrical transverse confinement across the sheet is provided by a vertically propagating focused pinning beam, with measured waists are $89.7\text{ }\mu\text{m}$ (in x) and $87.6\text{ }\mu\text{m}$ (in y), while the trapping frequency $\omega_1 \approx 2\pi \cdot 61 \pm 3\text{ Hz}$ was initially measured using the parametric heating method.

An additional linear external potential to induce Husimi oscillations is then formed magnetically using two approximately Helmholtz configured magnetic coils spaced evenly about the condensate. Modulating their electrical currents produces potentials of the form $V_B(x, t) = \mu_B g_F m_F b_x x \sin(t)$ given μ_B the Bohr magneton, g_F the Landé factor, and b_x the spatial gradient of the magnetic field amplitude along the x -direction. The (non-resonant) Husimi model fit to these experiments is

$$\xi(t) = \frac{\mu_B g_F m_F b_x}{m(\omega_1^2 - \omega_2^2)} \left[\sin(\omega_2 t) - \frac{\omega_2}{\omega_1} \sin(\omega_1 t) \exp(-\gamma t) \right]. \quad (6)$$

Trajectory damping, as quantified in the experiments by the parameter γ , is discussed shortly.

Husimi oscillations were induced using driving frequencies $\omega_2 \approx 2\pi \cdot 43.13\text{ Hz}$ which roughly correspond to $\omega_2/\omega_1 = 1/\sqrt{2}$, i.e. below the resonant (trapping) frequency. This produces aperiodic centre-of-mass trajectories [15], as shown in Fig. 2(a). These runs had atom numbers ranging between $N = (7.2 \pm 0.4) \times 10^4$ and $(3.4 \pm 0.1) \times 10^5$ and condensate fractions between $N_0/N = 0.47 \pm 0.05$ and 0.69 ± 0.08 . The data was extracted using 20 ms time-of-flight absorption imaging that destroys each BEC. Three data sets were recorded sequentially to evaluate consistency. Over several periods of modulation we observed no appreciable coupling of the centre-of-mass motion along x into the orthogonal (y) spatial direction in Fig. 2(b). We additionally observed no appreciable collective mode excitations, indicated by the approximately constant cloud radii over time (extracted from the optical dipole experiment as the Thomas-Fermi radius of the condensed atomic den-

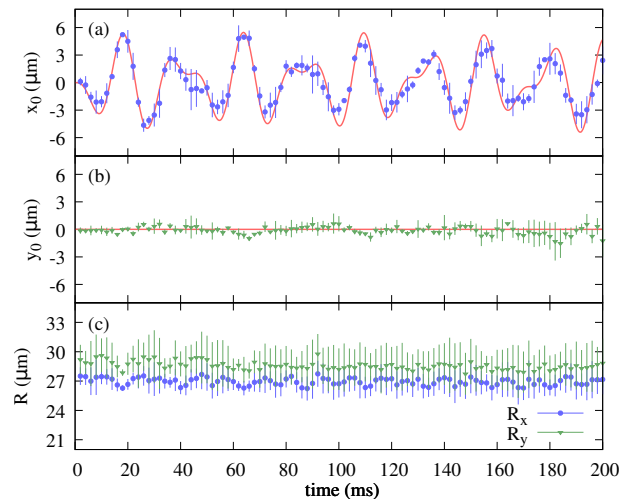


FIG. 2. (color online) Optical dipole experiment under Husimi driving with trap frequency of $\omega_1 \approx 2\pi \cdot 61 \pm 3\text{ Hz}$ and periodic driving frequency set to $\omega_2 = 2\pi \cdot 43.13\text{ Hz}$ to give an aperiodic trajectory. Panels (a),(b) show centre-of-mass measurements in the x - and y -direction, respectively. Panel (c) shows the cloud radius (R) measured in the x - and y -directions. Each data point is the average of three runs, with one standard deviation indicated by the error bars. The solid line in (a) shows the fit to Eqn. 6 with parameters: $\omega_1 = 2\pi \cdot 66.4 \pm 0.2\text{ Hz}$, $\omega_2 = 2\pi \cdot 43.13\text{ Hz}$ (fixed), $b_x = 0.93 \pm 0.03\text{ G/cm}$, $\gamma = 6.7 \pm 1.1\text{ s}^{-1}$.

sity distribution), as shown in Fig. 2(c).

We numerically fit to the experimental data in Fig. 2(a) to Eqn. 6, which shows an excellent fit consistent with our estimated parameters of the system (see caption). However, the estimated damping rate gives a decay time $1/\gamma = 150\text{ ms}$, so we performed additional experiments with times out past 1 s, where the centre-of-mass at these later times closely follows the driving oscillations (see Supplementary Figure 1 [47]), and a fit to this dataset gives a consistent estimate of $\gamma = 5.4 \pm 0.4\text{ s}^{-1}$.

We investigated the damping systematics by varying the condensate fraction, and changing the driving frequency to 86.27 Hz , above resonance. Fig. 3 shows the fitted values of the damping parameter, which is independent of driving frequency, but varies with condensate fraction. We attribute the damping of the Husimi oscillations within this trapping configuration to anharmonicity of the optical potential, from both the imperfections in the Gaussian beam, and the Gaussian form of the trap. 2-D calculations that mimic the experiment support this conclusion - see Supplementary Section 3 [47]. A lower condensate fraction indicates a larger thermal cloud, and atoms can potentially scatter between condensate modes and the thermal fraction due to the anharmonicity.

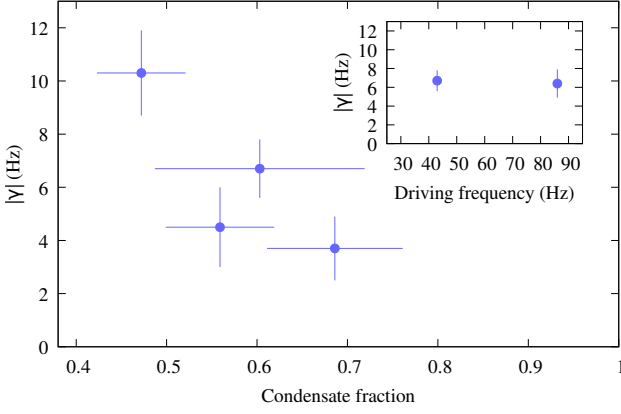


FIG. 3. (color online) Experimentally-observed damping in the optical dipole experiment under Husimi with trap frequency of $\omega_1 \approx 2\pi \cdot 61 \pm 3$ Hz. The damping rate, γ , is extracted from the fit to the experimental data using Eqn. 6. The main figure shows the result of varied condensate fraction N_0/N with a fixed driving frequency of $\omega_2 = 2\pi \cdot 43.13$ Hz. The inset shows an additional data point by driving at $\omega_2 = 2\pi \cdot 86.27$ Hz (also giving anharmonic motion) with a constant condensate fraction (≈ 0.6).

IV. EXPERIMENT II - ATOM CHIP

Our atom chip experiment is described in Refs. [50, 51]. It uses multiple independently-controlled wires to produce configurable magnetic potentials, $V(x, t) \approx c_2 x^2 + c_1(t)x$, where we choose by design to suppress higher-order terms here. This allows for the generation of both the oscillating linear term required for Husimi driving and a static harmonic trap, in contrast to the optical dipole trap. The atom chip forms condensates of ^{87}Rb containing approximately 10^4 atoms, with a high condensate fraction. The trap frequency of $\omega_x = 2\pi \cdot 8.545 \pm 0.003$ Hz was measured by rapidly turning on $c_1(t)$ from zero to a fixed value which shifts the location of the harmonic potential minimum, and observing subsequent coherent state oscillation.

The atom chip BEC was Husimi driven in the x -direction with driving frequency $\omega_2 = 2\pi \cdot 6.042$ Hz, and absorption imaged after 8 ms time-of-flight. Fig. 4 details the trajectories showing aperiodic motion (since $\omega_2/\omega_1 \approx 1/\sqrt{2}$). Four data sets were recorded sequentially to evaluate consistency, and error bars are shown but are mostly so small in Fig. 4(a) that they can not be seen. Note that outlying data resulting from sporadic issues during the condensate formation and imaging processes has been retained in Fig. 4. With no discernible damping ($\gamma \approx 0$) suggesting that the atom chip potential has minimised the anharmonic x^3, x^4, \dots terms.

Whilst the quality of the fitted model to the x motion is excellent, there are smaller oscillations in the transverse y -direction as shown in Fig. 4(b) that follow the driving frequency. Experimental field control limitations cause synchronous strong driving along the y direction, where

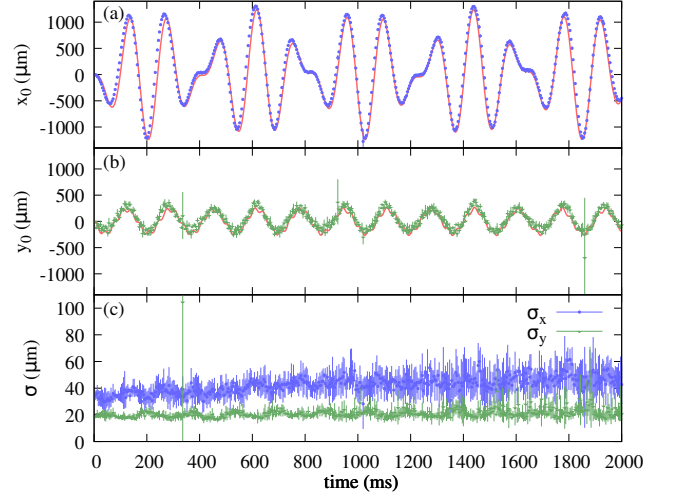


FIG. 4. (color online) Atom chip experiment under Husimi driving with trap frequency of $\omega_x \approx 2\pi \cdot 8.545 \pm 0.003$ Hz and periodic driving frequency set to $\omega_2 = 2\pi \cdot 6.042$ Hz to give an aperiodic trajectory. Panels (a),(b) show centre-of-mass measurements in the x - and y -direction, respectively. Panel (c) shows the cloud width measured in the x - and y -directions. The solid (red) line shows the fit to Eqn. 6 in (a) with $\omega_x = 2\pi \cdot 8.52 \pm 0.01$ Hz, $\omega_2 = 2\pi \cdot 6.08 \pm 0.01$ Hz, $b_x = 3.17 \pm 0.06$ G/cm, $\gamma = 0.00 \pm 0.02$ s $^{-1}$, whilst (b) has $\omega_y = 2\pi \cdot 29.98 \pm 0.01$ Hz, $\omega_2 = 2\pi \cdot 6.066 \pm 0.003$ Hz, $b_y = 23.8 \pm 0.6$ G/cm, with fixed $\gamma = 0$. The raw data from each of the four runs appears in Supplementary Fig. 5 [47].

fitting gives $b_y/b_x \approx 7.5$ with $\omega_y = 2\pi \cdot 29.98 \pm 0.01$ Hz, with driving $\omega_2 = 2\pi \cdot 6.066 \pm 0.003$ Hz. This is a ‘slow’ Husimi trajectory that follows the slower driving potential, with faster (and smaller) trap deviations superimposed on top that are hard to visually discern in Fig. 4(b). This allowed us to determine ω_y with a small uncertainty, finding that $\omega_y \gg \omega_x$ as per the atom chip design. Cloud widths, shown in Fig. 4(c), were extracted from the atom chip experiment using an in-plane 2-D Gaussian fit. The x -direction shows a growth trend over timescales of over a second, and minimal change in y . Given the quality of the desired x trajectory in Fig. 4(a), however, no further effort was made here to minimise the driving along the y direction and/or the growth trend in the x width.

V. APPLICATIONS OF HUSIMI DRIVING

Husimi driving allows for near-perfect condensate transport if the atoms are ‘caught’ at the stationary points where $\xi(t) = 0$. When driving on resonance these points occur when $f(t) = 0$, i.e. the linear potential is turned off. At this time the quadratic potential can be rapidly moved to $\xi(t)$ to catch the stationary atoms.

The proof-of-concept for this transport scheme using resonant Husimi driving was demonstrated in the atom chip experiment, as shown in Fig. 5(a) using $\omega_1 \approx 2\pi \cdot 8.545 \pm 0.003$ Hz and resonant driving frequency set to

$\omega_2 = 2\pi \cdot 8.545$ Hz. By rocking the atoms backwards then forwards the resonant motion predicted by Eqn. 5 is observed, including the linear increase in the oscillation amplitude (longer time data is shown in Supplementary Fig. 7 [47], showing 1 s of driving over distances spanning 4 mm, which is near the limit of the magnetic potential). We chose two points in the trajectory to catch the atoms by rapidly adjusting the potential (i.e. $c_1(t)$ from zero to the value that best moves the harmonic trap to the catch location). These are shown in Fig. 5(a) as the horizontal data points, which exhibit very little residual oscillation.

Stability of the y -trajectory is generally observed in both cases, whilst the widths are noisy over four data runs, but relatively constant as expected. The stability of the condensate after the shift of the static harmonic trap indicates that this procedure could be repeated from the new centre-of-mass position, allowing conveyor belt transport whilst maintaining the initial BEC state, e.g. over multiple elements for atomtronics. Near-resonant driving in the optical dipole experiment also performed as per Eqn. 5 (see Supplementary Fig. 4 [47]), and transport could be done here by suddenly translating the pinning laser using acousto-optic or spatial light modulators.

Quantifying transport speed for comparison across experimental systems requires an implementation-agnostic measure. We evaluate our speeds relative to the oscillator speed, which indicates the maximum speed at which the trap can be rigidly displaced without inducing excita-

tions in the trapped state - slow enough for transport to remain adiabatic throughout. ^{87}Rb atoms in a 8.545 Hz trap have an oscillator length $\beta = \sqrt{\hbar/m\omega} \approx 3.7 \mu\text{m}$ and oscillator period $T = 2\pi/\omega \approx 120$ ms, for an oscillator speed of $\beta/T \approx 30 \mu\text{m/s} = 0.03 \mu\text{m/ms}$. We define the transport speedup factor as the ratio of the average transport speed to the oscillator speed, allowing for comparisons between different transport protocols, trapping methods, and atomic species.

The Husimi-based transport in Fig. 5 has a transport speedup of 72 (data series ‘C1’). This is modest in relation to STA methods which have proposed/theoretical speedups of up to 1000 [32] – though experimental work has shown additional constraints are required to reduce excitation, resulting in implementation of transport with speedups in the range of 200 to 500 [43]. Our results, however, do not explore the limit of Husimi transport. By increasing the driving gradient, b_x , and driving frequency ω_2 in Eqn. 5, faster transport can be achieved. The centre-of-mass trajectory in Fig. 4 already indicates that a speedup of 270 is easily achievable in the existing atom chip apparatus by catching the condensate at the first maximum of the trajectory.

Another application, already demonstrated, is for *in-situ* trapping frequency measurement. For example, our fitting results shown in the caption of Fig. 2 give a more precise measure of the optical trap frequency compared to parametric heating, and can simultaneously quantify the magnetic field gradient and the presence of anharmonicity and noise through damping. To be useful, this method must provide higher accuracy in the trap frequency extraction from a similar amount of data, and we outline an approach for maximizing the precision of Husimi trajectory fits with minimal experimental data in Supplementary Section 4 [47]. In exploring future schemes, other driving functions $f(t)$ in Eqn. 2 have analytic or numerical solutions and provide alternate trajectories. When the harmonic potential can be moved, as in the atom chip experiment, Husimi driving gives a similar accuracy to just translating the potential and observing coherent oscillations (as per the atom chip experiment). Husimi driving thus provides a measure of the quality of control over an experimental system, similar to using Husimi driving to benchmark computational methods [12, 15].

We lastly propose the use of Husimi driving for atom interferometry experiments. The phase coherence of a condensate after Husimi driving can be established by interference with a reference condensate placed in a different spin-state. Furthermore, the separability of the Husimi solution in more than one dimension can be taken advantage of for atomic Sagnac interferometry in 3-D. Consider the generalised 3-D Husimi potential, $V_f(x, y, z, t) = \frac{1}{2}m\vec{\omega}^2\vec{r}^2 - \vec{A}_t\vec{r}$, where scalar parameters are replaced with vector quantities $\vec{\omega} = (\omega_x, \omega_y, \omega_z)$, $\vec{A}_t = (A_x \sin(\omega_{2,x}t), A_y \sin(\omega_{2,y}t), A_z \sin(\omega_{2,z}t))$, and $\vec{r} = (x, y, z)$. Lissajous-like trajectories can be engineered by adopting unequal driving frequencies along each dimension, including closed loops for Sagnac interferometry.

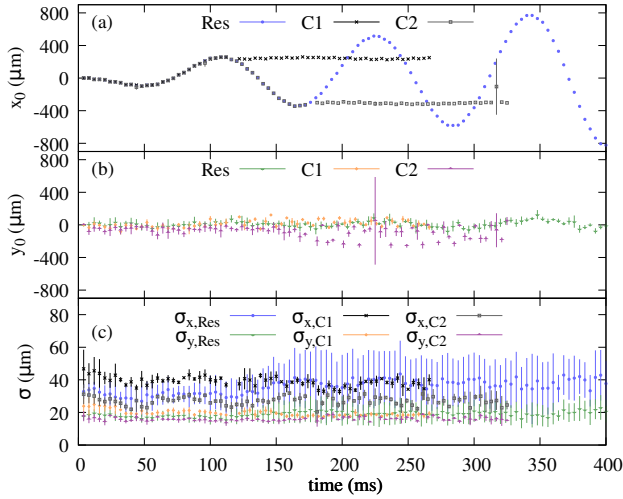


FIG. 5. (color online) Atom chip experiment for Husimi driven transport with trap frequency of $\omega_1 \approx 2\pi \cdot 8.545 \pm 0.003$ Hz and resonant driving frequency set to $\omega_2 = 2\pi \cdot 8.545$ Hz. Three experiments are shown — ‘Res’ is the resonant driving data runs that follows Eqn. 5, whilst ‘C1’ and ‘C2’ are the two transport runs that catch the atoms at the turning points. Panels (a),(b) show centre-of-mass measurements in the x - and y -direction, respectively. Panel (c) shows the cloud width (σ) measured in the x - and y -directions, with marker types and colours matching (a) and (b). The raw data for these experiments appears in Supplementary Fig. 6 [47].

This gives a similar scheme to that recently demonstrated by the group of Sackett *et al.* [52], and could also be performed with condensates in separate harmonic wells.

VI. CONCLUSIONS

We have demonstrated Husimi driving of a many-body system and shown that this driving provides a promising platform for the manipulation and study of BEC systems. Importantly, we have shown that Husimi driving can be achieved in both magneto-optical and purely magnetically trapped systems, and can be created in existing setups with minimal modification. Fast transport comparable to STA schemes can be readily achieved and, with further optimisation, higher speeds and excitation-free transport can be realised. Frequency fitting provides a sensitive, repeatable method for *in situ* measurement of harmonic trap frequencies without the need to squeeze or displace the trap. Additionally, the independence of our theoretical solution to inter-particle interactions indicates that Husimi oscillations can be induced in degenerate and/or thermal ensembles of trapped atoms (Bosonic or Fermionic). Note that the Husimi driving system, whilst integrable, does not constitute a time-

crystal (despite satisfying some of the properties when ω_2/ω_1 is a rational number). Overall, the Husimi driving scheme provides a promising new platform for high-precision BEC manipulation and new avenues to conduct one-body, few-body, and many-body experiments.

VII. ACKNOWLEDGMENTS

The authors would like to thank C.D. Jackson, O. Sandberg, T.W. Neely, and M.J. Davis for valuable discussions, and especially thank H. Rubinsztein-Dunlop for her support. This research was initiated through an Australian Research Council Future Fellowship (FT100100905), and supported by the Australian Research Council Centre of Excellence for Engineered Quantum Systems (EQUS, CE170100009). Numerical simulations were performed on The University of Queensland's School of Mathematics and Physics Core Computing Facility "getafix" (thanks to Dr. L. Elliott and I. Mortimer for computing support). A portion of this work was performed in the Space Vehicles Directorate of the US Air Force Research Laboratory with funding from the Air Force Office of Scientific Research (AFRL/AFOSR Lab Task 19RVCOR0499).

-
- [1] K. Husimi, Miscellanea in Elementary Quantum Mechanics, II, *Progress of Theoretical Physics* **9**, 381 (1953), with contributions noted from T. Taniuti, Y. Suzuki, T. Dodo, M. Ôtuka, R. Utiyama, and H. Arita.
 - [2] R. P. Feynman, Mathematical Formulation of the Quantum Theory of Electromagnetic Interaction, *Phys. Rev.* **80**, 440 (1950).
 - [3] A. M. Dykhne, Quantum transitions in the adiabatic approximation, *Sov. Phys. JETP* **11**, 411 (1960), *zh. Eksp. Teor. Fiz.* 38, 570 (1960).
 - [4] S. Solimeno, P. Di Porto, and B. Crosignani, Quantum Harmonic Oscillator with Time-Dependent Frequency, *J. Math. Phys.* **10**, 1922 (1969).
 - [5] V. S. Popov and A. M. Perelomov, Parametric Excitation of a Quantum Oscillator, *Sov. Phys. JETP* **29**, 738 (1969), *zh. Eksp. Teor. Fiz.* 56, 1375 (1969).
 - [6] M. A. Lohe, Exact time dependence of solutions to the time-dependent Schrödinger equation, *J. Math. Phys. A* **42**, 035307 (2009).
 - [7] M. Kleber, Exact solutions for time-dependent phenomena in quantum mechanics, *Phys. Rep.* **236**, 331 (1994).
 - [8] Y. Kagan, E. L. Surkov, and G. V. Shlyapnikov, Evolution of a bose-condensed gas under variations of the confining potential, *Phys. Rev. A* **54**, R1753 (1996).
 - [9] R. P. Feynman, An Operator Calculus Having Applications in Quantum Electrodynamics, *Phys. Rev.* **84**, 108 (1951).
 - [10] I. Fujiwara, Operator Calculus of Quantized Operator, *Prog. Theor. Phys.* **7**, 433 (1952).
 - [11] E. H. Kerner, Note on the Forced and Damped Oscillator in Quantum Mechanics, *Can. J. Phys.* **36**, 371 (1958).
 - [12] A. D. Bandrauk and H. Shen, Improved exponential split operator method for solving the time-dependent Schrödinger equation, *Chem. Phys. Lett.* **176**, 428 (1991).
 - [13] P. Hänggi, Driven Quantum Systems, Chap. 5, in [14] (1998).
 - [14] T. Dittrich, P. Hänggi, G. Ingold, B. Kramer, G. Schön, and W. Zwerger, eds., *Quantum Transport and Dissipation* (Wiley-Vch, Weinheim, 1998).
 - [15] C. D. Jackson, J. F. Corney, and M. W. J. Bromley, Benchmarking numerical solutions to the doubly-time-dependent Schrödinger equation (2021), in preparation.
 - [16] D. Guéry-Odelin, A. Ruschhaupt, A. Kiely, E. Torrontegui, S. Martínez-Garaot, and J. G. Muga, Shortcuts to adiabaticity: Concepts, methods, and applications, *Rev. Mod. Phys.* **91**, 045001 (2019).
 - [17] L. Amico, M. Boshier, G. Birkel, A. Minguzzi, C. Miniatura, L. Kwek, and et al, Roadmap on Atomtronics: State of the art and perspective, *AVS Quantum Sci.* **3**, 039201 (2021).
 - [18] M. Greiner, I. Bloch, T. W. Hänsch, and T. Esslinger, Magnetic transport of trapped cold atoms over a large distance, *Phys. Rev. A* **63**, 031401 (2001).
 - [19] W. Hänsel, J. Reichel, P. Hommelhoff, and T. W. Hänsch, Magnetic conveyor belt for transporting and merging trapped atom clouds, *Phys. Rev. Lett.* **86**, 608 (2001).
 - [20] S. Minniberger, F. Diorice, S. Haslinger, C. Hufnagel, C. Novotny, N. Lippok, J. Majer, C. Koller, S. Schneider, and J. Schmiedmayer, Magnetic conveyor belt transport of ultracold atoms to a superconducting atomchip, *Applied Physics B* **116**, 1017 (2014).

- [21] T. Badr, D. B. Ali, J. Seaward, Y. Guo, F. Wiotte, R. Dubessy, H. Perrin, and A. Perrin, Comparison of time profiles for the magnetic transport of cold atoms, *Appl. Phys. B* **125**, 102 (2019).
- [22] J. Han, X. Xu, H. Zhang, and Y. Wang, Optimal transport of cold atoms by modulating the velocity of traps, *Chin. Phys. B* **22**, 023702 (2013).
- [23] D. Chen, H. Zhang, X. Xu, T. Li, and Y. Wang, Nonadiabatic transport of cold atoms in a magnetic quadrupole potential, *Appl. Phys. Lett.* **96**, 134103 (2010).
- [24] S. Schmid, G. Thalhammer, K. Winkler, F. Lang, and J. Hecker Denschlag, Long distance transport of ultracold atoms using a 1D optical lattice, *New J. Phys.* **8**, 159 (2006).
- [25] G. Ness, C. Shkedrov, Y. Florshaim, and S. Y. Realistic shortcuts to adiabaticity in optical transfer, *New J. Phys.* **20**, 095002 (2018).
- [26] A. Couvert, T. Kawalec, G. Reinaudi, and D. Guéry-Odelin, Optimal transport of ultracold atoms in the non-adiabatic regime, *EPL (Europhysics Letters)* **83**, 13001 (2008).
- [27] T. L. Gustavson, A. P. Chikkatur, A. E. Leanhardt, A. Görlitz, S. Gupta, D. E. Pritchard, and W. Ketterle, Transport of bose-einstein condensates with optical tweezers, *Phys. Rev. Lett.* **88**, 020401 (2001).
- [28] J. Léonard, M. Lee, A. Morales, T. M. Karg, T. Esslinger, and T. Donner, Optical transport and manipulation of an ultracold atomic cloud using focus-tunable lenses, *New Journal of Physics* **16**, 093028 (2014).
- [29] T. Middelmann, S. Falke, C. Lisdat, and U. Sterr, Long-range transport of ultracold atoms in a far-detuned one-dimensional optical lattice, *New. J. Phys.* **14**, 073020 (2012).
- [30] D. Chen, M. White, C. Borries, and B. DeMarco, Quantum Quench of an Atomic Mott Insulator, *Phys. Rev. Lett.* **106**, 235304 (2011).
- [31] E. Torrontegui, S. Ibáñez, X. Chen, A. Ruschhaupt, D. Guéry-Odelin, and J. G. Muga, Fast atomic transport without vibrational heating, *Phys. Rev. A* **83**, 013415 (2011).
- [32] E. Torrontegui, X. Chen, M. Modugno, S. Schmidt, A. Ruschhaupt, and J. G. Muga, Fast transport of Bose-Einstein condensates, *New J. Phys.* **14**, 013031 (2012).
- [33] E. Torrontegui, S. Martínez-Garaot, A. Ruschhaupt, and J. G. Muga, Shortcuts to adiabaticity: Fast-forward approach, *Phys. Rev. A* **86**, 013601 (2012).
- [34] X. Chen, R. Jiang, J. Li, Y. Ban, and E. Y. Sherman, Inverse engineering for fast transport and spin control of spin-orbit-coupled Bose-Einstein condensates in moving harmonic traps, *Phys. Rev. A* **97**, 013631 (2018).
- [35] Q. Zhang, X. Chen, and D. Guéry-Odelin, Fast and optimal transport of atoms with nonharmonic traps, *Phys. Rev. A* **92**, 043410 (2015).
- [36] U. Hohenester, P. Rekdal, A. Borzi, and J. Schmiedmayer, Optimal quantum control of Bose-Einstein condensates in magnetic microtraps, *Phys. Rev. A* **75**, 023602 (2007).
- [37] D. Guéry-Odelin and J. G. Muga, Transport in a harmonic trap: Shortcuts to adiabaticity and robust protocols, *Phys. Rev. A* **90**, 063425 (2014).
- [38] S. Deffner, C. Jarzynski, and A. del Campo, Classical and Quantum Shortcuts to Adiabaticity for Scale-Invariant Driving, *Phys. Rev. X* **4**, 021013 (2014).
- [39] Q. Zhang, J. G. Muga, D. Guéry-Odelin, and X. Chen, Optimal shortcuts for atomic transport in anharmonic traps, *J. Phys. B* **49**, 125503 (2016).
- [40] S. Amri, R. Corgier, D. Sugny, E. M. Rasel, N. Gaaloul, and E. Charron, Optimal control of the transport of Bose-Einstein condensates with atom chips, *Sci. Rep.* **9**, 5346 (2019).
- [41] O. Mandel, M. Greiner, A. Widera, T. Rom, T. W. Hänsch, and I. Bloch, Coherent transport of neutral atoms in spin-dependent optical lattice potentials, *Phys. Rev. Lett.* **91**, 010407 (2003).
- [42] A. Browaeys, H. Häffner, C. McKenzie, S. L. Rolston, K. Helmerson, and W. D. Phillips, Transport of atoms in a quantum conveyor belt, *Phys. Rev. A* **72**, 053605 (2005).
- [43] R. Corgier, S. Amri, W. Herr, H. Ahlers, J. Rudolph, D. Guéry-Odelin, E. M. Rasel, E. Charron, and N. Gaaloul, Fast manipulation of Bose-Einstein condensates with an atom chip, *New J. Phys.* **20**, 055002 (2018).
- [44] J. F. Dobson, Harmonic-Potential Theorem: Implications for Approximate Many-Body Theories, *Phys. Rev. Lett.* **73**, 2244 (1994).
- [45] S. Friebe, C. D'Andrea, J. Walz, M. Weitz, and T. W. Hänsch, CO₂-laser optical lattice with cold rubidium atoms, *Phys. Rev. A* **57**, R20 (1997).
- [46] B. D. Esry, Hartree-Fock theory for Bose-Einstein condensates and the inclusion of correlation effects, *Phys. Rev. A* **55**, 1147 (1997).
- [47] See Supplemental Material at [URL will be inserted by publisher] for technical details.
- [48] T. A. Bell, J. A. P. Glidden, L. Humbert, M. W. J. Bromley, S. A. Haine, M. J. Davis, T. W. Neely, M. A. Baker, and H. Rubinsztein-Dunlop, Bose-Einstein condensation in large time-averaged optical ring potentials, *New J. Phys.* **18**, 035003 (2016).
- [49] T. A. Bell, G. Gauthier, T. W. Neely, H. Rubinsztein-Dunlop, M. J. Davis, and M. A. Baker, Phase and micro-motion of Bose-Einstein condensates in a time-averaged ring trap, *Phys. Rev. A* **98**, 013604 (2018).
- [50] J. A. Stickney, E. Imhof, B. Kasch, B. Kroese, J. A. R. Crow, S. E. Olson, and M. B. Squires, Tunable axial potentials for atom-chip waveguides, *Phys. Rev. A* **96**, 053606 (2017).
- [51] M. B. Squires, S. E. Olson, B. Kasch, J. A. Stickney, C. J. Erickson, J. A. R. Crow, E. J. Carlson, and J. H. Burke, Ex vacuo atom chip Bose-Einstein condensate, *Appl. Phys. Lett.* **109**, 264101 (2016).
- [52] E. R. Moan, R. A. Horne, T. Arpornthip, Z. Luo, A. J. Fallon, S. J. Berl, and C. A. Sackett, Quantum Rotation Sensing with Dual Sagnac Interferometers in an Atom-Optical Waveguide, *Phys. Rev. Lett.* **124**, 120403 (2020).

Supplementary: Husimi-driven many-body systems realised with Bose-Einstein condensates

B.J. Mommers,^{1,2} A. Pritchard,^{1,2} T.A. Bell,^{1,2} R.N. Kohn, Jr.,³ S.E. Olson,⁴ M. Baker,^{5,2,1} and M.W.J. Bromley^{6,2}

¹*Centre for Engineered Quantum Systems, The University of Queensland, St Lucia, Australia*

²*School of Mathematics and Physics, The University of Queensland, St Lucia, Australia*

³*Space Dynamics Laboratory, Albuquerque, New Mexico 87106, USA*

⁴*Air Force Research Laboratory, Kirtland AFB, New Mexico 87117, USA*

⁵*Quantum Technologies, Cyber and Electronic Warfare Division,
Defence Science and Technology Group, Brisbane, Australia*

⁶*School of Sciences, University of Southern Queensland, Toowoomba, Australia*

I. NON-LINEAR SCHRÖDINGER EQUATION THEORY

In this section we derive the solution to the Gross-Pitaevskii equation (GPE) under Husimi driving and show that the result is independent of both the interaction term in the GPE and the initial state in the static harmonic trap. These attributes allow arbitrary harmonically-trapped states of a Bose-Einstein condensate (BEC) to be driven under this scheme. The Husimi “see-saw” potential is a type of forced harmonic oscillator which is described using,

$$V(x, t) = \frac{1}{2}m\omega_1^2 x^2 - Axf(t) \equiv \frac{1}{2}m\omega_1^2 \left(x - \frac{Af(t)}{m\omega_1^2} \right)^2 - \frac{A^2 f^2(t)}{2m\omega_1^2}, \quad (1)$$

where ω_1 represents the (fixed) trapping frequency of the time-independent harmonic trapping component, $f(t)$ is an arbitrary modulation function, and A is the modulation amplitude. Husimi’s original solution describes the driving of a wavefunction in a harmonic trap under the Schrödinger equation [1]. We instead consider single-particle dynamics governed by the Gross-Pitaevskii equation (GPE), a nonlinear Schrödinger equation (NLSE),

$$i\hbar \frac{\partial}{\partial t} \psi(x, t) = \left(-\frac{\hbar^2}{2m} \frac{\partial^2}{\partial x^2} + V(x, t) + g|\psi(x, t)|^2 \right) \psi(x, t), \quad (2)$$

where m is the atomic mass, the external potential $V(x, t)$ is described by Eqn. 1. The 1-D nonlinear interaction strength $g \propto g_{3D}$, the 3-D strength, where $g_{3D} = 4\pi\hbar^2 a_s(N-1)/m$, which depends on the s -wave atom-atom scattering length (a_s), and the number of other atoms ($N-1$) in the condensate [2]. This is then a single particle model, where $\int |\psi(x, t)|^2 dx = 1$ is the chosen normalisation.

Following Husimi’s method, we perform a coordinate transformation $x \rightarrow (x - \xi(t)) = x'$, where ξ is an arbitrary function of time only. Expressing the NLSE in terms of this new coordinate gives,

$$i\hbar \frac{\partial}{\partial t} \psi(x' + \xi, t) = \left(i\hbar \dot{\xi} \frac{\partial}{\partial x'} - \frac{\hbar^2}{2m} \frac{\partial^2}{\partial x'^2} + \frac{m}{2} \omega_1^2 (x' + \xi)^2 - A(x' + \xi)f(t) + g|\psi(x' + \xi, t)|^2 \right) \psi(x' + \xi, t). \quad (3)$$

As an ansatz, the solution is factored into the product of a phase and arbitrary function $\varphi(x' + \xi, t)$, taking the form,

$$\psi(x' + \xi, t) = \exp \left(\frac{im\dot{\xi}x'}{\hbar} \right) \varphi(x' + \xi, t). \quad (4)$$

We insert this into the coordinate-transformed NLSE, which gives

$$\begin{aligned} i\hbar \frac{\partial}{\partial t} \varphi(x' + \xi, t) = & -\frac{\hbar^2}{2m} \frac{\partial^2}{\partial x'^2} \varphi(x' + \xi, t) + \frac{m}{2} \omega_1^2 x'^2 \varphi(x' + \xi, t) + g|\varphi(x' + \xi, t)|^2 \varphi(x' + \xi, t) \\ & + \left[m\ddot{\xi} + m\omega_1^2 \xi - Af(t) \right] x' \varphi(x' + \xi, t) \\ & + \left(-\frac{m}{2} \dot{\xi}^2 + \frac{m}{2} \omega_1^2 \xi^2 - A\xi f(t) \right) \varphi(x' + \xi, t). \end{aligned} \quad (5)$$

By constraining ξ to satisfy the classical equation of motion for a forced oscillator $m\ddot{\xi} + m\omega_1^2 \xi = Af(t)$, the term in square brackets above is reduced to zero, and ξ can be physically interpreted as the centre-of-mass coordinate $\langle x \rangle$.

As in Husimi's original derivation, the term within parentheses in Eqn. 5 above can be reduced to zero by performing the additional factorisation,

$$\varphi(x' + \xi, t) = \phi(x' + \xi, t) \cdot \exp \left(\frac{i}{\hbar} \int_0^t \frac{1}{2} m \dot{\xi}^2 - \frac{m}{2} \omega_1^2 \xi^2 + A \xi f(t) dt \right). \quad (6)$$

To see the effect this factorisation has on the transformed NLSE of Eqn. 5, we calculate the relevant derivatives,

$$\begin{aligned} \frac{\partial}{\partial t} \varphi(x' + \xi, t) &= i\hbar \frac{\partial \phi(x' + \xi, t)}{\partial t} \cdot \exp \left(\frac{i}{\hbar} \int_0^t \frac{m}{2} \dot{\xi}^2 - \frac{m}{2} \omega_1^2 \xi^2 + A \xi f(t) dt \right) \\ &\quad - \left(\frac{m}{2} \dot{\xi}^2 - \frac{m}{2} \omega_1^2 \xi^2 + A \xi f(t) \right) \phi(x' + \xi, t) \cdot \exp \left(\frac{i}{\hbar} \int_0^t \frac{m}{2} \dot{\xi}^2 - \frac{m}{2} \omega_1^2 \xi^2 + A \xi f(t) dt \right), \end{aligned} \quad (7)$$

$$\frac{\partial^2}{\partial x'^2} \varphi(x' + \xi, t) = \frac{\partial^2 \phi(x' + \xi, t)}{\partial x'^2} \cdot \exp \left(\frac{i}{\hbar} \int_0^t \frac{m}{2} \dot{\xi}^2 - \frac{m}{2} \omega_1^2 \xi^2 + A \xi f(t) dt \right), \quad (8)$$

and substitute them back into the transformed NLSE. We then obtain,

$$\begin{aligned} i\hbar \frac{\partial \phi(x' + \xi, t)}{\partial t} \cdot \exp \left(\frac{i}{\hbar} \int_0^t L dt \right) &= -\frac{\hbar^2}{2m} \frac{\partial^2 \phi(x' + \xi, t)}{\partial x'^2} \cdot \exp \left(\frac{i}{\hbar} \int_0^t L dt \right) + \frac{m}{2} \omega_1^2 x^2 \phi(x' + \xi, t) \cdot \exp \left(\frac{i}{\hbar} \int_0^t L dt \right) \\ &\quad + g |\phi(x' + \xi, t)|^2 \phi(x' + \xi, t) \cdot \exp \left(\frac{i}{\hbar} \int_0^t L dt \right) \\ &\quad + \left[m \ddot{\xi} + m \omega_1^2 \xi - A f(t) \right] x' \phi(x' + \xi, t) \cdot \exp \left(\frac{i}{\hbar} \int_0^t L dt \right) \\ &\quad + \left(-\frac{m}{2} \dot{\xi}^2 + \frac{m}{2} \omega_1^2 \xi^2 - A \xi f(t) \right) \phi(x' + \xi, t) \cdot \exp \left(\frac{i}{\hbar} \int_0^t L dt \right) \\ &\quad + \left(\frac{m}{2} \dot{\xi}^2 - \frac{m}{2} \omega_1^2 \xi^2 + A \xi f(t) \right) \phi(x' + \xi, t) \cdot \exp \left(\frac{i}{\hbar} \int_0^t L dt \right), \end{aligned} \quad (9)$$

where $L = \frac{m}{2} \dot{\xi}^2 - \frac{m}{2} \omega_1^2 \xi^2 + A \xi f(t)$. The global phase factor $\exp(\frac{i}{\hbar} \int_0^t L dt)$ can be eliminated, and by applying the constraint on ξ , our result is the NLSE in terms of $\phi(x, t)$ within a static harmonic potential (changing $\partial/\partial x' \rightarrow \partial/\partial x$),

$$i\hbar \frac{\partial \phi(x, t)}{\partial t} = -\frac{\hbar^2}{2m} \frac{\partial^2 \phi(x, t)}{\partial x^2} + \frac{m}{2} \omega_1^2 x^2 \phi(x, t) + g |\phi(x, t)|^2 \phi(x, t). \quad (10)$$

Note this result does not depend on the form of the interaction term $g |\phi(x' + \xi, t)|^2$. To satisfy Eqn. 10, ϕ must be *any* solution to the NLSE for a static harmonic potential (including time-dependent solutions), which takes the form $\phi(x, t) \equiv \chi(x - \xi, t)$. This gives our final result: BEC states confined using the Husimi see-saw potential in Eqn. 1 satisfy

$$\psi(x, t) = \chi(x - \xi, t) \cdot \exp \left(\frac{im \dot{\xi}(x - \xi)}{\hbar} + \frac{i}{\hbar} \int_0^t \frac{1}{2} m \dot{\xi}^2 - \frac{m}{2} \omega_1^2 \xi^2 + A \xi f(t) dt \right). \quad (11)$$

This solution results in the centre-of-mass coordinate being translated according to $\xi(t)$, and the local evolution of the state about the centre-of-mass evolving according to the dynamics of the state χ in a stationary harmonic trap.

These results also hold for the full 3-D NLSE as the the Husimi-driving will not excite additional modes. If $\chi(x, y, z, t)$ begins in an NLSE eigenstate at $t = 0$ then the mean-field potential, $g' |\chi(x - \xi, y, z, t)|^2$, is constant such that the dynamics all remain solely along the x -direction. If it is not in an initial eigenstate then the NLSE solution $\chi(x - \xi, y, z, t)$ will undergo dynamics in the x -direction that couple energy into/out of transverse modes, but these are not affected by the Husimi driving energy into/out of the collective wavefunction. If the initial state is excited/sloshing then the correspondence between the measurement of $\langle x \rangle(t)$ and $\xi(t)$ needs to be tempered by any local centre-of-mass dynamics of the condensate.

The initial motivation to investigate the above analytic solution to the NLSE was provided by an (unpublished) NLSE computational methods report by Luo [3], which relied on Bandrauk and Shen's numerical work [4], which, in turn, cites Husimi [1]. Luo, however, only considered the squeezing potential, $V(r, t) = \frac{1}{2} r^2 (1 + A \sin(\omega t))$ to explore time-dependent numerical solutions. Our theory here provides for an exacting test for non-linear Schrödinger equation computational modelling, beyond the linear [5].

II. HUSIMI DRIVING OF MANY-BODY SYSTEMS

The main result of the previous section provides a solution to the GPE under Husimi driving, and shows that condensates described by the GPE can be prepared in arbitrary states of a harmonic trap and have their centre-of-mass driven whilst local evolution is unaffected by driving. GPE dynamics assume a homogeneous zero-temperature gas of particles in the ground state, with interactions dominated by s -wave scattering. This is a good approximation for very low temperature condensates. However, experimental realisations of BECs include a thermal component due to imperfect evaporation. Nevertheless, the result of the previous section can readily be generalised to an interacting many-body Hamiltonian for N particles under Husimi driving. In this section we briefly show that the interaction-independence of the GPE result extends to many-body systems with arbitrary interaction potentials.

The Hamiltonian describing a many-body system, within the external potential Eqn. 1, takes the (1-D) form

$$H = \sum_{j=1}^N \left(\frac{-\hbar^2}{2m} \frac{\partial^2}{\partial x_j^2} + \frac{1}{2} m \omega_1^2 x_j^2 - A x_j f(t) + \sum_{k \neq j}^N V_{\text{int}}(x_j, x_k) \right), \quad (12)$$

where V_{int} is an arbitrary interaction potential describing pairwise interparticle interactions (and not double counting). Performing the change of coordinates $x_j \rightarrow (x_j - \xi(t)) = x'_j$ we obtain the many-body Schrödinger equation,

$$\begin{aligned} \sum_{j=1}^N i\hbar \frac{\partial}{\partial t} \psi(x'_j + \xi, t) = \sum_{j=1}^N \left(i\hbar \dot{\xi} \frac{\partial}{\partial x'_j} - \frac{\hbar^2}{2m} \frac{\partial^2}{\partial x_j'^2} + \frac{1}{2} m \omega_1^2 (x'_j + \xi)^2 - A(x'_j + \xi) f(t) + \xi, t \right) \\ + \sum_{k \neq j}^N V_{\text{int}}(x'_j + \xi, x'_k + \xi) \right) \psi(x'_j + \xi, t). \end{aligned} \quad (13)$$

The form of this transformed Hamiltonian shows that each particle in an arbitrary many-body state under Husimi driving evolves locally (with respect to the centre-of-mass motion) as if in a static harmonic trap, whilst being translated according to the classical forced oscillator solution. For an experimental BEC, this results in co-driving of both the condensate and any thermal cloud, indicating that driving will not induce additional heating, atom loss, or other excitations.

The Husimi-based solution to Eqn. 13 was also derived by Dobson in his development of the many-body Harmonic Potential Theorem (HPT) [6]. The HPT generalises the generalised Kohn theorem (GKT) to describe the dynamics of many-body interacting systems in an eigenstate of a harmonic scalar potential [6]. By performing the same coordinate transformation to that used by Husimi, the solution to the GKT Hamiltonian for interacting gases in a harmonic potential with a uniform linear field can be separated into the relative motion of the centre-of-mass and the stationary many-body eigenstate — the main result of the HPT. The HPT is obtained as a reduction from our present work, as the HPT, as presented, was restricted to the initial many-body state being an eigenstate. Dobson's 1994 paper, however, makes no reference to the 1953 (single particle) solution of Husimi [1].

III. PHENOMENOLOGICAL DAMPING OF HUSIMI TRAJECTORIES

The lack of damping in the all-magnetic atom chip experimental trajectories, as shown in Fig. 4 of the main text via the fitted $\gamma = 0.00 \pm 0.02 \text{ s}^{-1}$, indicates that the finite temperature of a condensate in the lab does not result in damping by itself. This is in agreement with the many-body theoretical result (above) where Husimi driving dynamics apply equally to condensed and thermal atoms.

In contrast, our optical dipole experimental investigation was initially unable to observe Husimi driving due to a poor optical pinning beam spatial distribution. Several improvements later the first signatures of Husimi oscillations were observed, although still very evidently damped over short time-scales. At this point the damped analytical expression for the centre of mass trajectory was conceived (Eqn. 6 in the main text), which then subsequently helped quantify the benefits of subsequent experimental changes to reduce the damping. As shown in Figs. 2 and 3 of the main text, damping was improved enough to observe Husimi driving, but remains significant, and looks to be independent of driving frequency but strongly dependent on temperature. The temperature-dependence was experimentally tested by varying the evaporation process to prepare clouds with different condensate fractions and therefore temperatures. These optical dipole results remain anomalous and need an explanation.

We decided to perform additional optical dipole experiments, going out beyond 1 second of driving time. Supplemental Fig. 1 shows very clearly the effect of damping over such long times; the centre-of-mass trajectory begins by

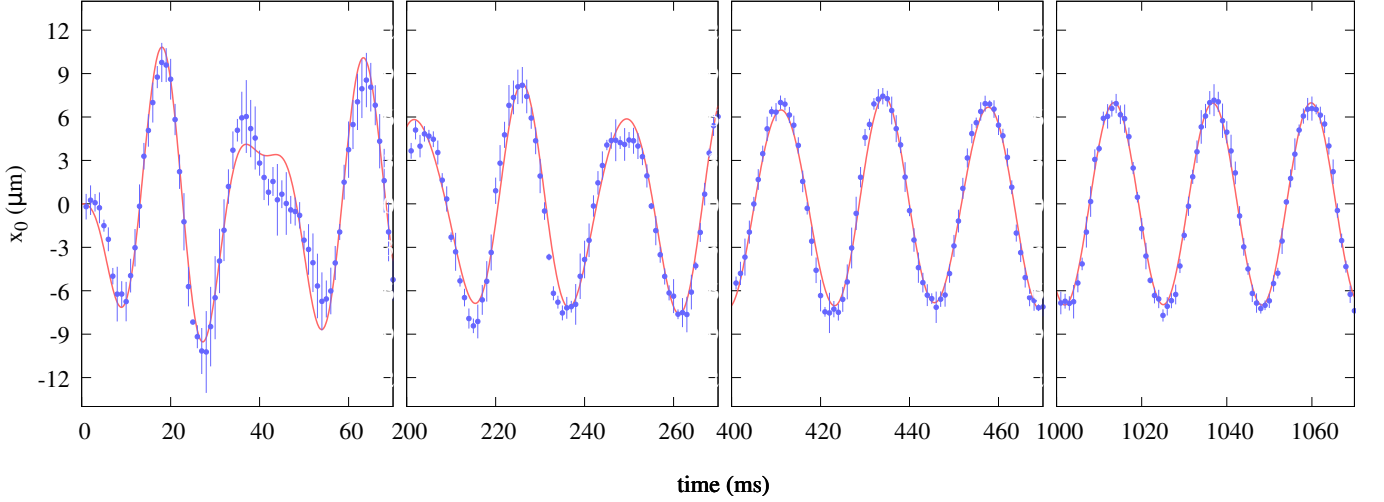


Figure 1. (color online) Optical dipole experiment under Husimi driving with trap frequency of $\omega_1 \approx 2\pi \cdot 61 \pm 3$ Hz and periodic driving frequency set to $\omega_2 = 2\pi \cdot 43.13$ Hz to give an initial aperiodic trajectory that then shows damping of the trajectory towards the driving frequency. The experimental configuration in these experiments is slightly different to those in Fig. 2 of the main text, with a stronger magnetic field driving larger spatial oscillations. The data was taken over 70 ms windows after driving for $\{0, 200, 400, 1000\}$ ms to assess the long-time effects of damping on trajectories. Only shown here are the centre-of-mass measurements in the x -direction. Each data point is the average of three runs, with one standard deviation indicated by the error bars. The solid (red) line shows the fit over the entire dataset (to Eqn. 6 in the main text) with parameters: $\omega_1 = 2\pi \cdot 67.43 \pm 0.06$ Hz, $\omega_2 = 2\pi \cdot 43.17 \pm 0.01$ Hz, $b_x = 2.30 \pm 0.03$ G/cm, $\gamma = 5.4 \pm 0.4$ s $^{-1}$.

following the Husimi solution until it evolves to follow the driving frequency at long times. (c.f. Fig. 2 of the main text).

To understand this further we have explored the optical dipole trapping system numerically, and show here that anharmonic noise/spatial distortions across the Gaussian potential reproduce the order of magnitude of the experimentally observed damping behaviour. Two effects were initially suspected: (1) imperfect beam propagation through the experimental optical system, and (2) the Gaussian pinning beam intensity profile itself. These are the two most conspicuous sources of anharmonicity explored numerically.

Several numerical potentials based on the experimental parameters were constructed to explore various damping contributions in isolation. An experimentally representative distorted Gaussian potential, $V_{\text{Experiment}}$, was firstly constructed using the experimentally measured optical intensity profile; the intensity distribution was measured using our standard $M = 6.38$ vertical imaging system and Prosilica EC380 camera. A purely Gaussian potential V_{Gaussian} was constructed by taking the numerical regression with $V_{\text{Experiment}}$, viz.

$$V_{\text{Gaussian}}(x, y) = -V_0 \exp\left(-\frac{2(x - x_0)^2}{w_x^2}\right) \exp\left(-\frac{2(y - y_0)^2}{w_y^2}\right), \quad (14)$$

where $V_0 = 3480$ nK and the widths, w , chosen to match the experiment (i.e. to match the pinning beam widths given in the main text, and the frequency as determined by parametric heating, 61 Hz).

This allows us to approximate the residual corrugations as $V_{\text{Noise}} = V_{\text{Experiment}} - V_{\text{Gaussian}}$, which contains amplitudes of order $\sim 0.05V_0$. Furthermore, an idealised harmonic potential V_{Harmonic} based on the quadratic fit to V_{Gaussian} was constructed to enable the gradual introduction of the higher-order anharmonic distortions (and provided an initial means to evaluate the adequate convergence of our numerical results against the exact analytic results). Finally, a corrugated harmonic potential was introduced $V_{\text{Corrugated}} = V_{\text{Harmonic}} + V_{\text{Noise}}$.

Two-dimensional Gross-Pitaevskii simulations were performed using the XMDS2 numerical integration package [7]. These simulations adopted a 1024×1024 point spatial lattice which spanned ± 34.304 μm along the x and y -dimensions. Dynamical processes along the third z -dimension were neglected given that comparatively tight confinement ($\omega = 2\pi \cdot 140$ Hz) was provided by the sheet potential, rather than the pinning beam ($\omega_1 \approx 2\pi \cdot 61$ Hz). Effectively zero-temperature condensates with chemical potential $\mu = 80$ nK and thus $N = 2.2 \times 10^5$ atoms were prepared using imaginary time methods, which gives the initial ($t = 0$) wavefunction. The Husimi driving potential was chosen to have field gradient $b_x = 1.04$ G/cm, with frequency $\omega_2 = 43.13$ Hz (giving dynamics similar to Fig. 2 in the main text). Our Husimi simulations used the fourth-order Runge-Kutta (RK4) algorithm and 1 μs fixed integration time-steps.

The Husimi damping strength associated with the distortions introduced by the optical system or associated with the Gaussian beam profile were investigated using the dimensionless parameters δ and β , through the continuously variable potentials,

$$V(\delta) = (1 - \delta)V_{\text{Harmonic}} + \delta V_{\text{Corrugated}} \quad , \quad V(\beta) = (1 - \beta)V_{\text{Harmonic}} + \beta V_{\text{Gaussian}} \quad . \quad (15)$$

Having run each δ or β simulation, we fit to the trajectories, and extract the estimated amount of damping.

Our quantitative damping results, based on the optical dipole experiment, are compiled in Supplemental Fig. 2. Firstly, we note that the simple phenomenological model introduced in Eqn. 6 in the main text appears to well describe both systems as the anharmonicities are introduced. The effect of the noise through δ is an order of magnitude larger than the inclusion of the Gaussian anharmonicity (x^3 , x^4 etc) through β . This suggests that it is the laser corrugation noise that dominates the damping of Husimi centre-of-mass oscillations in our optical dipole experiment. We observe the corrugation noise induced damping increase up towards 3 Hz which is consistent with the experimental values (see Fig. 3 of the main text). Pleasingly, the calculations show that only a small damping is introduced though the inclusion of the Gaussian anharmonicity, which suggests that our Gaussian laser potential is harmonic enough to observe Husimi driving — as we did in the optical dipole experiments. Also, x^3 and x^4 terms can be easily engineered in the atom chip experiment, but this was not done here.

Furthermore, in the simulations for $\delta > 0.3$ we observe a breakdown in the simple behaviour - the damping rate reduces whilst we observe increasing centre-of-mass oscillations in the direction transverse to the drive, induced by the measured noise profile present in the experimental apparatus. This regime requires further investigation to understand, but was initially suspected to be numerical of origin as more highly-excited modes are initially created in the wavefunction at $t = 0$, and then even more are generated by the time-dependent scattering of the wavefunction as it is driven through the static, yet noisy, corrugated potential. The grid effectively places an upper limit of the excitations that can be generated in the calculation, however, running simulations with 2048×2048 grid points and timesteps of 316 ns and 100 ns does not change these $\delta > 0.3$ results. We speculate that the temperature-dependence of damping (as shown in Fig. 3 of the main text) is due to the coupling of such collective excitations to the thermal cloud which is co-oscillating with the condensate through the corrugated potential in the experiment. This would require modelling beyond the Gross-Pitaevskii Equation (Eqn. 2).

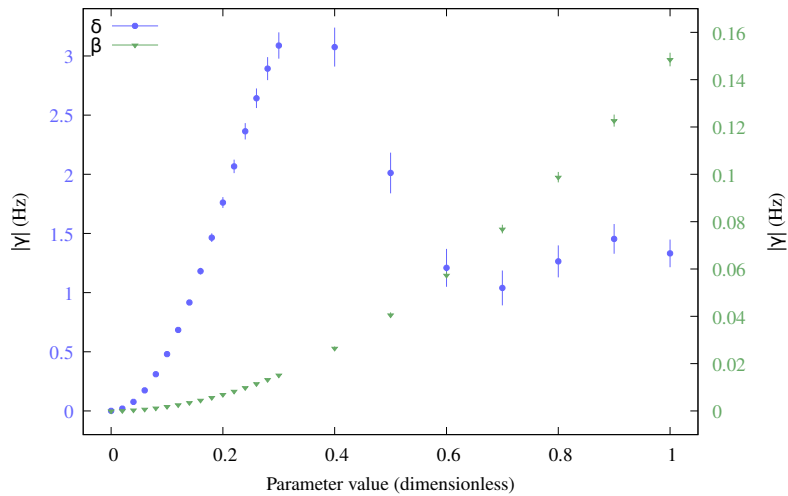


Figure 2. (color online) Simulation of the optical dipole experiment exploring the effect of trap anharmonicity on damping of simulated trajectories using two different sets of potentials as per Eqn. 15. Parameter δ (blue circles, left vertical axis) interpolates between a smooth harmonic trap at $\delta = 0$ and a corrugated harmonic trap with experimentally-observed deformation profile and amplitude at $\delta = 1$; distortions with amplitudes up to of order $\sim 0.05V_0$ are introduced for $\delta = 1$, where $V_0 = 3480$ nK represents the Gaussian potential depth. Parameter β (green triangles, right vertical axis) interpolates between an ideal harmonic trap at $\beta = 0$ and an ideal Gaussian trap at $\beta = 1$. Error bars indicate uncertainty in the best fit to simulated trajectories. Note the use of two different scales for the y -axes. For further calculation details see the corresponding text.

IV. HUSIMI TRAJECTORIES FOR TRAP FREQUENCY MEASUREMENT

Whilst Husimi trajectory fitting allows for determination of trap frequency, its utility in practice requires accurate and precise measurement with a minimal number of data points. In this section we consider a method for making optimal use of the analytic solution for the centre-of-mass trajectory when determining trap frequency. The variation in the trajectory $\xi(t)$ as trap frequency changes is given by the derivative,

$$\frac{\partial \xi}{\partial \omega_1} = \frac{A}{m(\omega_1^2 - \omega_2^2)} \left[\frac{1}{\omega_1} \left(\frac{\omega_2}{\omega_1} \sin(\omega_1 t) - \omega_2 t \cos(\omega_1 t) \right) - \frac{2}{(\omega_1^2 - \omega_2^2)} \left(\sin(\omega_2 t) - \frac{\omega_2}{\omega_1} \sin(\omega_1 t) \right) \right]. \quad (16)$$

The $-\omega_2 t \cos(\omega_1 t)$ term in this expression indicates that deviations in the trap frequency produce more distinguishable trajectories at later times, therefore late-time measurements should allow for more precise frequency fitting. However, condensate lifetime and imperfections in the experimental implementation of Husimi driving will constrain the maximum duration for which the state is preserved. Therefore we propose a method for making optimal use of the known analytic solution for improving trap frequency measurement precision.

First, estimate the trap frequency based on known experimental parameters. Then compare the analytic trajectory at this frequency to trajectories for nearby trap frequencies, such as in Supplemental Fig. 3. This allows identification of regions in which features are qualitatively distinguishable for small variations in trap frequency. Trajectory data should be focused around these features to constrain the fit. For similar parameter values as used in the optical dipole trap experiments in the main text, Supplemental Fig. 3 indicates that sub-Hz precision can be achieved by focusing data collection around specific regions of the trajectory, before the trajectories diverge with time.

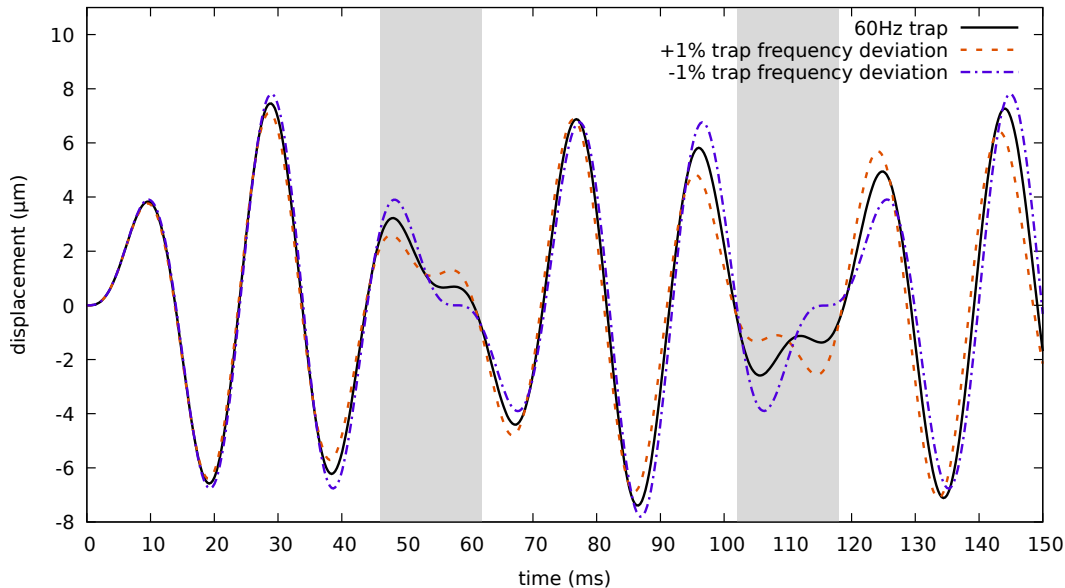


Figure 3. (color online) Analytic trajectories for Husimi driving at fixed driving frequency $\omega_2 = 2\pi \cdot 43.134$ Hz with driving amplitude $A = 1.0$ G/cm and varying trap frequencies $\omega_1 = 2\pi \times 60$ Hz with a 1% deviation. Features around $t \approx 55$ ms and 115 ms (indicated by grey shaded regions) could be used to increase fit precision due to the higher distinguishability of features in the trajectory.

V. ADDITIONAL EXPERIMENTAL DATA

We wrap up this supplemental paper with an additional experiment that was performed in the optical dipole experiment, and then present two sets of original datapoints for the atom chip experiments, and a final extended experimental atom chip dataset.

A single set of near-resonant driving runs with the optical dipole experiment is shown in Supplemental Fig. 4. There is a small amount of cross-coupling of the direction of Husimi driving into the transverse direction. Driving close to the trap frequency increases the displacement at turning points in the trajectory and ensures the magnetic field gradient is flat at those turning points, creating ideal conditions to rapidly move the centre of the harmonic trap to the new location to enable the transport and relocation of a cloud of atoms. In the current experimental setup we were unable to rapidly move the laser (which could simply be achieved with an Acousto-Optic Modulator Device or a Spatial Light Modulator), and instead we demonstrated quantum transport in the configurable atom chip device (see Fig. 5 in the main text).

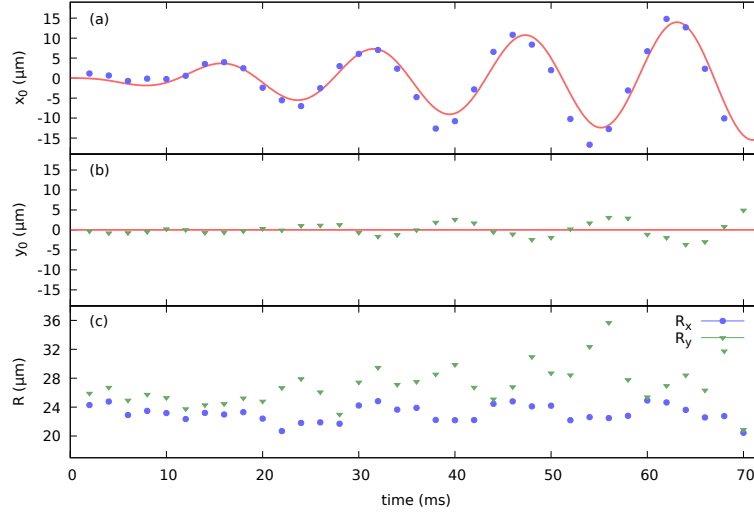


Figure 4. (color online) Optical dipole experiment under near-resonant Husimi driving with trap frequency of $\omega_1 \approx 2\pi \cdot 61 \pm 3$ Hz and periodic driving frequency set to $\omega_2 = 2\pi \cdot 64$ Hz to give a near-periodic trajectory. Panels (a),(b) show centre-of-mass measurements in the x - and y -direction, respectively. Panel (c) shows the cloud radius (R) measured in the x - and y -directions. Each data point is the average of three runs, with one standard deviation indicated by the error bars. The solid line in (a) shows the fit to Eqn. 6 of the main text with parameters: $\omega_1 = 2\pi \cdot 61.9 \pm 4.8$ Hz, $\omega_2 = 2\pi \cdot 64.9 \pm 6.7$ Hz, $b_x = 0.566 \pm 0.041$ G/cm, $\gamma = 5.2 \pm 18$ s $^{-1}$.

The four data series taken in the atom chip experiment to obtain the aperiodic Husimi trajectories for $\omega_2/\omega_1 \approx 1/\sqrt{2}$ driving (see Fig. 4 of the main text) are given in Supplemental Fig. 5. Strong agreement in the trajectories and only gradual long-term broadening of the cloud are observed. A small number of outliers by the centre-of-mass position in the y -direction. A gradual broadening of the cloud over long times (many driving periods) is present in some of the datasets used, which is captured by the averaged data presented in Fig. 4 of the main text.

The four data series taken in the atom chip experiment to obtain the periodic Husimi trajectories for $\omega_2/\omega_1 \approx 1$ driving (see Fig. 5 of the main text) are given in Supplemental Fig. 6. Four data series were averaged for the resonant driving shown, and three data series were averaged for each of the transport protocol demonstrations. It is hard to see the different data points in Fig. 6(a) but they are there - indicating the robustness of the driving and transport scheme. No broadening of the cloud width is observed for the runs in which the cloud was caught at a turning point in the trajectory to achieve transport.

Finally, an extended time-series of the resonantly-driven atom chip dataset is provided in Supplemental Fig. 7, which includes and extends the data in Supplemental Fig. 6, (and thus also includes and extends beyond the 'Res' data shown in Fig. 5 of the main text). Some outlying points in the x -trajectory, in addition to substantial broadening of the cloud after multiple resonant driving periods are observed in some of the datasets. Impressively, the resonant driving in the atom chip is able to extend to transport over distances of over 4 mm, which is 100 times larger than the cloud width, and beyond which the limit of the atom chip potential control lies.

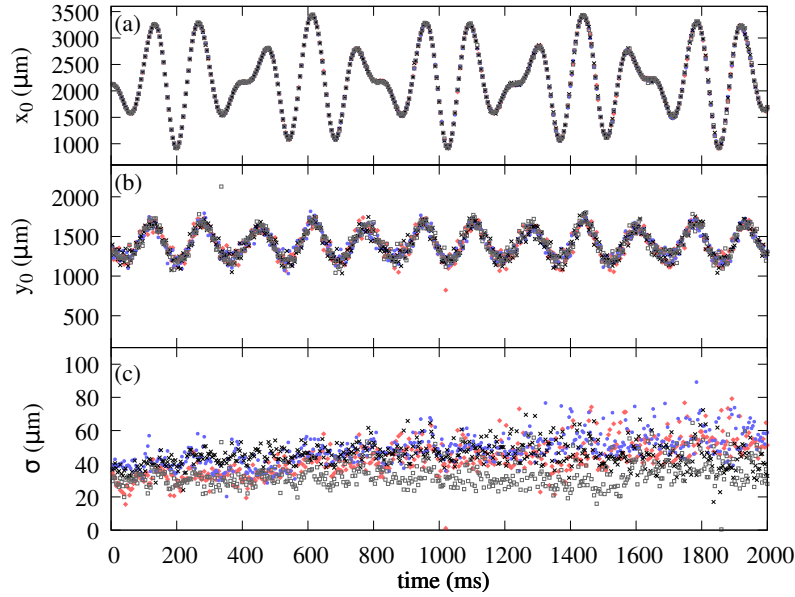


Figure 5. (color online) Atom chip experiment under Husimi driving with trap frequency of $\omega_1 \approx 2\pi \cdot 8.545 \pm 0.003$ Hz and periodic driving frequency set to $\omega_2 = 2\pi \cdot 6.042$ Hz to give an aperiodic trajectory. Panels (a),(b) show centre-of-mass measurements in the x - and y -direction, respectively. Panel (c) shows the cloud width measured in the x - and y -directions. Note that the panel (b) scale is different to panel (a). The averaged data from each of these four runs appears in Fig. 4 of the main text.

-
- [1] K. Husimi, Miscellanea in Elementary Quantum Mechanics, II, *Progress of Theoretical Physics* **9**, 381 (1953), with contributions noted from T. Taniuti, Y. Suzuki, T. Dodo, M. Ôtuka, R. Utiyama, and H. Arita.
 - [2] B. D. Esry, Hartree-Fock theory for Bose-Einstein condensates and the inclusion of correlation effects, *Phys. Rev. A* **55**, 1147 (1997).
 - [3] C. Luo, Modeling Bose-Einstein condensate with Gross-Pitaevskii equation, *preprint* (2009).
 - [4] A. D. Bandrauk and H. Shen, Higher order exponential split operator method for solving time-dependent Schrödinger equations, *Can. J. Chem.* **70**, 555 (1992).
 - [5] C. D. Jackson, J. F. Corney, and M. W. J. Bromley, Benchmarking numerical solutions to the doubly-time-dependent Schrödinger equation (2021), in preparation.
 - [6] J. F. Dobson, Harmonic-Potential Theorem: Implications for Approximate Many-Body Theories, *Phys. Rev. Lett.* **73**, 2244 (1994).
 - [7] G. R. Dennis, J. J. Hope, and M. T. Johnsson, XMDS2: Fast, scalable simulation of coupled stochastic partial differential equations, *Comp. Phys. Comm.* **184**, 201 (2013).

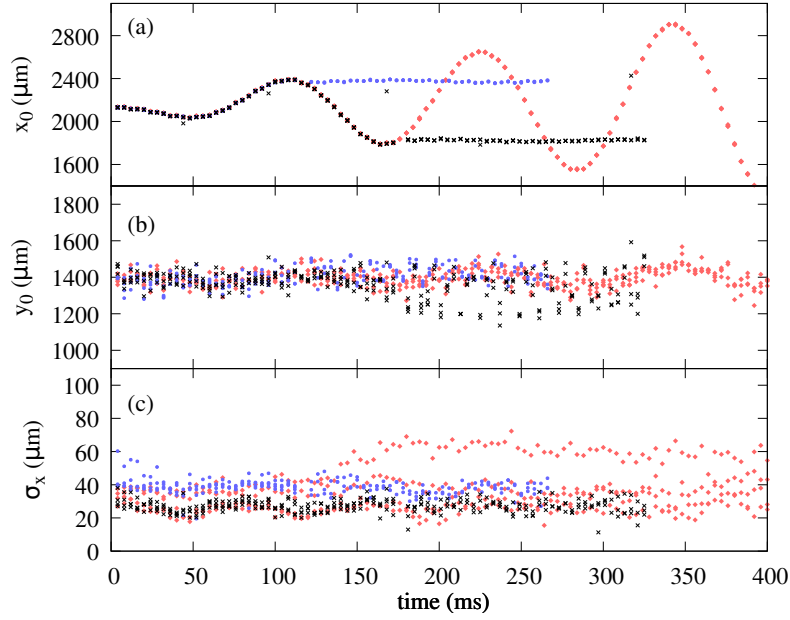


Figure 6. (color online) Atom chip experiment for Husimi driven transport with trap frequency of $\omega_1 \approx 2\pi \cdot 8.545 \pm 0.003$ Hz and resonant driving frequency set to $\omega_2 = 2\pi \cdot 8.545$ Hz. Three experiments are shown — red data points are the four resonant driving data runs (see Eqn. 5 in the main text), whilst the blue and black are the two transport experiments that catch the atoms at the turning points, each consisting of three data runs. Panels (a),(b) show centre-of-mass measurements in the x - and y -direction, respectively. Panel (c) shows the cloud width (σ_x) measured in the x -direction, with marker types and colours matching (a) and (b). Note that the panel (b) scale is different to panel (a). The averaged data from each of these four or three runs appears as ‘Res’, ‘C1’, and ‘C2’ in Fig. 5 of the main text.

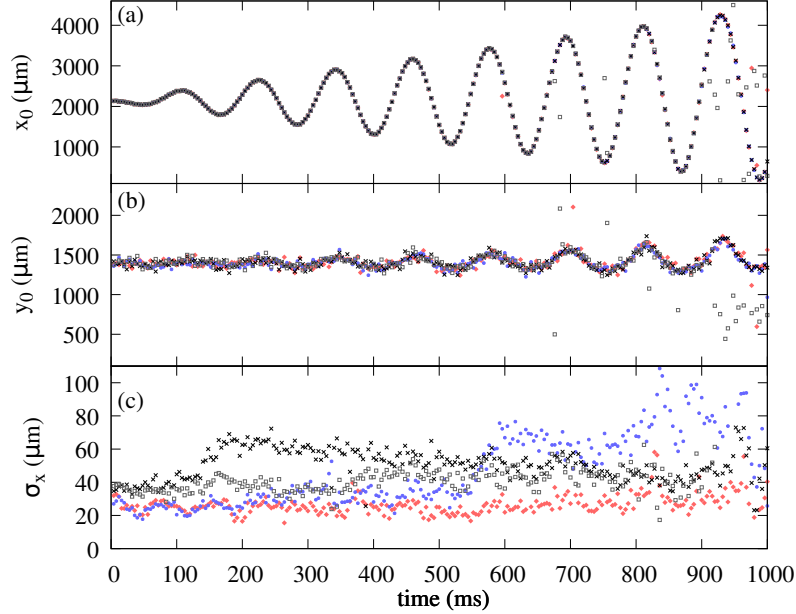


Figure 7. (color online) Atom chip experiment for Husimi driven transport with trap frequency of $\omega_1 \approx 2\pi \cdot 8.545 \pm 0.003$ Hz and resonant driving frequency set to $\omega_2 = 2\pi \cdot 8.545$ Hz. The data points in different colours are the four resonant driving data runs (see Eqn. 5 in the main text). Panels (a),(b) show centre-of-mass measurements in the x - and y -direction, respectively. Panel (c) shows the cloud width (σ_x) measured in the x -direction, with marker types and colours matching (a) and (b). Note that the panel (b) scale is different to panel (a). The averaged data from each of these four runs appears as ‘Res’ in Fig. 5 of the main text (and unaveraged in Supplemental Fig. 6), however, here the experiment times were pushed out to 1 s.